SCIENCE CHINA
Information Sciences

• RESEARCH PAPER •

March 2024, Vol. 67, Iss. 3, 132301:1–132301:16
https://doi.org/10.1007/s11432-023-3919-2

Blindness-free beam scanning antenna with array of array architecture: principle, design, and experiment

Jianxu SUN & Yujian CHENG*

School of Electronic Science and Engineering, University of Electronic Science and Technology of China, Chengdu 611731*, China*

Received 29 September 2023/Revised 1 December 2023/Accepted 18 December 2023/Published online 20 February 2024

Abstract This paper presents a 66–76-GHz sparsely-excited phased array antenna with the array of array (AoA) architecture for eliminating the blindness and suppressing the grating lobe when scanning. For the array antennas printed on the thick dielectric layers with high relative permittivity, scanning blindness appears and seriously impacts the radiation performance. To address this issue, the AoA topology is developed first. It finds that the scanning blindness appears due to the coupling of the radiating Floquet modes to the non-radiating surface wave (SW) modes. Therefore, the array is divided into two types of domino subarrays. The inner-phase distributions are introduced into the domino subarrays to break the one-to-one relationship between the Floquet mode and the SW mode. Then, the blindness inside $\pm 60^\circ$ scanning volume is eliminated by the aperiodic subarrays. Meanwhile, the aperiodic inner-phase distributions enhance the aperiodicity of the array and contribute to suppressing the grating lobe when scanning. Next, the meta-surface-based dipole with the shorted post is chosen as the unit cell for the proposed aperiodic array. Based on these methods, the array achieves the wide-scanning performance of $\pm 60^\circ$ in the E-plane and $\pm 30^\circ$ in the H-plane, without the blindness and the grating lobe. Finally, the 16×16 array is built and simulated with the dimension of 32 mm × 32 mm. At the highest operating frequency, the simulated gains are 28.42, 25.17, and 24.01 dBi when scanning to the broadside, 50° in the E-plane, and 30° in the H-plane, respectively. Compared to the ideal gain, it shows that the simulated radiation efficiency is about 84.13%, 62.08%, and 35.23% when scanning to the broadside, 50° in the E-plane, and 30° in the H-plane, respectively. The worst transmission coefficient, i.e., the worst isolation, is -11.97 dB between the central element and its two adjacent elements in the E-plane. The array prototypes are fabricated, and the experiments are carried out to verify the correctness of the principle and design. Compared to existing antenna array designs, due to the employment of the AoA architecture, the proposed antenna achieves 51.30% channel reduction with both blindness-free and grating-lobe-free performance. Meanwhile, due to the regular and periodic subarray spacing, the best realizability is achieved for the sparsely-excited phased array at the millimeter-wave bands. This is valuable for the wide-scanning phased array antennas in the sixth-generation (6G) highly-integrated communication systems at the millimeter-wave bands.

Keywords 6G communication systems, phased array, AoA, aperiodic subarray, wideband, wide-scanning, surface-wave, scanning blindness, grating lobe

1 Introduction

Wireless communication technology in the millimeter-wave frequency bands is emerging as a cutting-edge frontier that holds the potential to enable a higher data rate, lower latency time, and larger system capacity. In sixth-generation (6G) wireless communication systems, to meet the requirement of delivering multi-Gbps to simultaneous multiusers, a sufficiently wide spectrum resource is essential [1–3]. Therefore, millimeter-wave frequency bands such as the E-band from 60 to 90 GHz are selected as potential candidates [4–7]. Antennas play a pivotal role in establishing the connection between wireless communication systems. To create connectivity between the base stations and terminal users flexibly and rapidly, wideband and wide-scanning phased arrays are necessary. However, as the operating frequency increases, the physical dimensions of the antenna decrease, which increases the complexity of integrating antennas with the active components. It can also render some fabrication processes, such as the wire electrical

* Corresponding author (email: chengyujian@uestc.edu.cn)

discharge machining and computer numerical control machining processes, unsuitable for utilization in the millimeter-wave frequency range [8–10]. In this situation, multilayer and high-integration fabrication processes are required to integrate the antennas, the power dividers, and the active devices in the compact package [11–16].

Various types of antennas using different fabrication processes and materials for 6G and millimeter-wave spectrum are developed intensively, such as antenna on chip (AoC) and antenna in package (AiP) in both single and array configurations [17–23]. The AoC technologies eliminate the need for wire bonding or ball grid array (BGA) [24] and close the gap between the antenna and the active component, which reduces insertion loss. Compared to AoC technologies, AiP technologies provide a low-cost solution for the high-integration radio frequency front end. It usually employs fabrication processes such as the low temperature cofired ceramic (LTCC) process [25,26], the printed circuit board (PCB) process [27,28], and the embedded wafer level packaging (EWLP) process [29]. However, for the directional-radiation array with the metal reflector (ground plane) in the dielectric-filled package, the transverse magnetic (TM) and transverse electric (TE) surface waves (SWs) can be excited along this grounded dielectric layer. As studied in [30], scanning blindness occurs when the propagation constant of the SW mode matches the correlative Floquet mode over the array aperture. At the blindness, the radiation pattern of the array and the active voltage standing wave ratio (VSWR) will deteriorate unacceptably. This leads to limited scanning volume for both the AoC and the AiP.

In past years, several methods were developed to eliminate this type of scanning blindness [31–37]. Periodic electromagnetic bandgap (EBG) materials, including the grounded dielectric rods [31], mushroom-like structures [32, 33], uniplanar compact structures [34], and air-filled perforations [35–37], are investigated to address this issue, through their well-designed forbidden gap at the operating frequency bands. However, these materials suffer from bulky structures or the particular fabrication process, which makes them difficult to use in the large-scale phased array at the millimeter-wave bands. In [38], the effect of the subarray configurations on the scanning blindness shows that the properly spaced subarrays can almost eliminate blindness caused by the SWs. However, the grating lobe angles will move toward the broadside with the increase in the element spacing, also accounting for the resultant limited scanning range. Recently, the unconventional phased array architecture with the sparsely-excited array topology was studied [39–44]. In these situations, the antenna elements will be positioned with different classes, such as the active elements, the inactive elements, the vacant elements, the shifted elements, and the combined elements. It is similar to making a rearranged array of the phased array, which can be described as an array of array (AoA). The antenna with the AoA architecture, consisting of the aperiodic subarrays with the irregular shapes [39–42] or inner-phase distributions [43, 44], is adopted to suppress the grating lobes when scanning. Indeed, the irregular shapes of the subarray work against the realizability of the large-scale phased array at the millimeter-wave bands. For the AoA architecture with the inner-phase distributions in the subarrays, it is still hoped that the lesser phase-shifting subarrays in the whole array will reduce the additional insertion loss induced by the phase-shifting networks.

In addition to the scanning blindness caused by SWs that can degrade the antenna radiation performance, the mutual coupling between antenna elements will also result in distortion of the element pattern, the degradation of the active VSWR, and consequently, lead to distortion of the synthesized beam of phased-array antennas and reduced radiation efficiency [45–48]. In addition to the mentioned EBG materials, there are some mutual coupling reduction technologies such as the decoupling feeding network [49], the decoupling surface [50–52], the mode cancellation [53–57], the mode separation [58], the employment of a circulator [59], and field confinement [60]. The above methods provide some efficient solutions to reduce the mutual coupling between antenna elements. However, it also escalates the complexity of design and integration, with some applicable only to smaller arrays composed of several antennas.

In this paper, a 66–76-GHz, sparsely-excited phased array antenna is proposed with the AoA architecture for blindness-free and grating-lobe-free scanning performance. The principle of scanning blindness in the PCB-based millimeter-wave antenna is studied and analyzed first. Then, the wideband dipole element is carefully designed based on the infinite array simulation, which takes into account factors such as mutual coupling and the parasitic reactance between the antenna elements. The meta-surface (MS)-based impedance matching layer and the shorted post are added into the dipole element to improve impedance matching and eliminate the distortion of the element pattern caused by the mutual coupling. Next, two types of domino subarrays with and without inner-phase distributions are employed in the aperiodic array to eliminate the scanning blindness caused by the SWs. Compared to the traditional

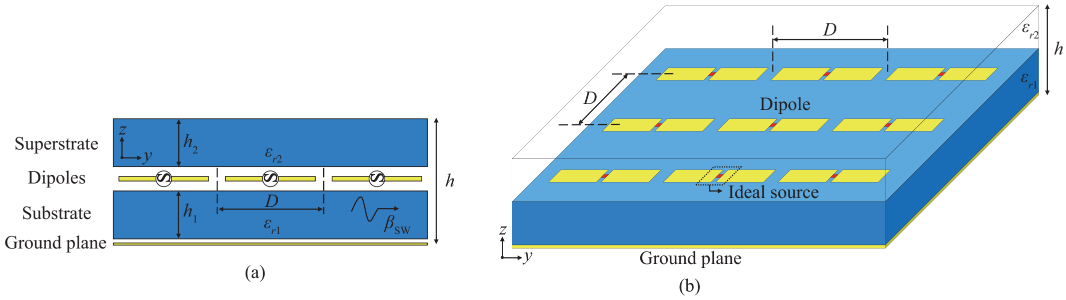

Figure 1 (Color online) Antenna array printed on grounded dielectric layers. (a) Side view; (b) trimetric view.

array topology optimization model, the influence of the inner-phase distributions for the equivalent phase centers is taken into account. Therefore, the array topology obtained by the improved algorithm model can efficiently suppress the SWs and grating lobes inside the scanning volume efficiently over all of the operating frequency bands. Finally, the 16 × 16 array prototypes are fabricated and measured, which shows the correctness of the principle and design.

2 Principle of scanning blindness in PCB-based millimeter-wave antenna

2.1 Coupling from radiating Floquet modes to non-radiating SW modes

The multi-layer PCB process provides excellent integration capacity for the millimeter-wave package. In terms of a wideband phased array antenna, a thick enough substrate is required to maintain impedance bandwidth [61]. Sometimes, an additional superstrate is also needed to improve the impedance matching when scanning [35–37]. In the actual antenna fabrication process, the planar metal structures such as the antenna radiator and ground plane are printed on the surface of the laminate layer through processes like exposure, development, and etching. The three-dimensional structures like antenna feedlines are achieved through processes like plated-through-hole metallization. Then, the multiple laminate layers are bonded together using the prepreg layers through a multi-layer lamination process, completing the printing of the antenna. To simplify the analysis, the dipole radiators fed with the ideal sources, i.e., without considering the feedlines, are adopted as shown in Figure 1. Figure 1(b) shows the geometry of the infinite dipole array with the ideally excited dipoles printed on the grounded dielectric (the superstrate is filled with the transparent color for clarity). Then, the thickness of the metal and prepreg layers is ignored to obtain the uniform environment filled with the grounded dielectric layers. Here, h_1, h_2, ε_{r1} and ε_{r2} are the thickness and the relative permittivity of the dielectric layers, respectively. h is the total thickness of the dielectric layers above the ground plane. D is the element spacing of the radiators along the x- and y-direction. It defines the effective relative permittivity $\varepsilon_{r,\mathrm{eff}}$ of the whole array, which can be expressed by

$$\varepsilon_{r,\mathrm{eff}} = \frac{\varepsilon_{r1}h_1 + \varepsilon_{r2}h_2}{h}. \tag{1}$$

Notably, in the analysis process for the excited SWs in the grounded dielectric layers when scanning, the mutual coupling between antenna elements is not critical and is therefore neglected here. However, in contrast, it is essential to focus on the coupling between radiating Floquet modes and non-radiating SW modes. According to the array theory [62], the Floquet mode propagation constant vector can be expressed as

$$\boldsymbol{k}_{mn} = k_0\left(\frac{m\lambda_0}{D} + u\right)\boldsymbol{x} + k_0\left(\frac{n\lambda_0}{D} + v\right)\boldsymbol{y}, \tag{2a}$$

$$u = \cos\phi_0\sin\theta_0 \text{ and } v = \sin\phi_0\sin\theta_0. \tag{2b}$$

Here, (θ_0, ϕ_0) is the array scan angle and λ_0 is the free-space wavelength at the operating frequency. k_0 is the free-space wavenumber at the operating frequency. m and n are the Floquet mode indexes. At the same time, the SWs with the TE and TM modes can be excited in the equivalent single grounded dielectric layer with the thickness h and the relative permittivity $\varepsilon_{r,\mathrm{eff}}$, where the propagation constant of the SWs $\beta_{\mathrm{SW}} \geqslant k_0$ [30]. To extract β_{SW}, it assumes that the electric field $E_y(x,y,z)$ and magnetic $H_y(x,y,z)$

of the SWs propagates in the y-direction with an $\mathrm{e}^{-\mathrm{j}\beta y}$ propagation factor and has no variation in the x-direction ($\frac{\partial}{\partial x}=0$), i.e., $E_y(x,y,z)=e_y(x,z)\,\mathrm{e}^{-\mathrm{j}\beta y}$ and $H_y(x,y,z)=h_y(x,z)\,\mathrm{e}^{-\mathrm{j}\beta y}$. Then, considering the Helmholtz wave equation in each region as shown in Figure 1(a), it can be separately expressed for the TM mode SWs and TE mode SWs as

$$\left(\frac{\partial^2}{\partial z^2}+\varepsilon_{r,\mathrm{eff}}k_0^2-\beta_{\mathrm{SW,TM}}^2\right)e_y(x,z)=0, \qquad \text{for } 0\leqslant z\leqslant h, \tag{3a}$$

$$\left(\frac{\partial^2}{\partial z^2}+k_0^2-\beta_{\mathrm{SW,TM}}^2\right)e_y(x,z)=0, \qquad \text{for } z\geqslant h, \tag{3b}$$

$$\left(\frac{\partial^2}{\partial z^2}+\varepsilon_{r,\mathrm{eff}}k_0^2-\beta_{\mathrm{SW,TE}}^2\right)h_y(x,z)=0, \qquad \text{for } 0\leqslant z\leqslant h, \tag{3c}$$

$$\left(\frac{\partial^2}{\partial z^2}+k_0^2-\beta_{\mathrm{SW,TE}}^2\right)h_y(x,z)=0, \qquad \text{for } z\geqslant h. \tag{3d}$$

It defines the cutoff wavenumbers k_1 and k_2 in the dielectric layers ($0\leqslant z\leqslant t$) and the free-space above the superstrate ($z\geqslant t$), respectively. k_1 and k_2 can be expressed as

$$k_1^2=\varepsilon_{r,\mathrm{eff}}k_0^2-\beta_{\mathrm{SW}}^2, \tag{4a}$$

$$k_2^2=\beta_{\mathrm{SW}}^2-k_0^2, \tag{4b}$$

$$k_1^2+k_2^2=(\varepsilon_{r,\mathrm{eff}}-1)k_0^2. \tag{4c}$$

Then, the general solutions for (3) are

$$e_y(x,z)=A_1\sin k_1z+B_1\cos k_1z, \qquad \text{for } 0\leqslant z\leqslant h, \tag{5a}$$

$$e_y(x,z)=C_1\mathrm{e}^{k_2z}+D_1\mathrm{e}^{-k_2z}, \qquad \text{for } z\geqslant h, \tag{5b}$$

$$h_y(x,z)=A_2\sin k_1z+B_2\cos k_1z, \qquad \text{for } 0\leqslant z\leqslant h, \tag{5c}$$

$$h_y(x,z)=C_2\mathrm{e}^{k_2z}+D_2\mathrm{e}^{-k_2z}, \qquad \text{for } z\geqslant h. \tag{5d}$$

In (5), $A_{1,2}$, $B_{1,2}$, $C_{1,2}$, and $D_{1,2}$ are the constants. To obtain k_1 and k_2, the relation between the electric field $\boldsymbol{E}$ and magnetic field $\boldsymbol{H}$ of the TM and the TE SWs, derived by the Maxwell equations, is employed together with the electromagnetic field boundary conditions on the surface of the layered medium and the radiation condition [63]. Therefore, the relation between k_1 and k_2 can be expressed as

$$k_1\tan k_1h=\varepsilon_{r,\mathrm{eff}}k_2, \qquad \text{for TM mode}, \tag{6a}$$

$$-k_1\cot k_1h=k_2, \qquad \text{for TE mode}. \tag{6b}$$

By simultaneously solving (4c) and (6), k_1, k_2, and β_{SW} can be extracted. For more intuition, the graphical method can be used by transforming (4c) as

$$(k_1h)^2+(k_2h)^2=(\varepsilon_{r,\mathrm{eff}}-1)(k_0h)^2. \tag{7}$$

Eq. (7) shows the circle equation whose center is located at the origin of the customized coordinate system, with the radius equal to $\sqrt{\varepsilon_{r,\mathrm{eff}}-1}(k_0h)$. k_1h and k_2h represent the horizontal and vertical axis for the customized coordinate system, respectively. Here, $k_2h=\frac{k_1h}{\varepsilon_{r,\mathrm{eff}}}\tan k_1h$ for the TM mode and $k_2h=-k_1h\cot k_1h$. Using the coordinate of the intersection between the circle equation and the k_2h equations, k_1 and k_2 are obtained and then the the propagation constant β_{SW} can be calculated by (4a) or (4b). When the Floquet mode propagation constant of the array matches the propagation constant β_{SW}, the SWs appear and the input power of the antenna elements cannot efficiently radiate out. The angle of the scanning blindness can be calculated by

$$\left(\frac{\beta_{\mathrm{SW}}}{k_0}\right)^2=\left(\frac{m\lambda_0}{D}+u_{\mathrm{SW}}\right)^2+\left(\frac{n\lambda_0}{D}+v_{\mathrm{SW}}\right)^2, \tag{8a}$$

$$u_{\mathrm{SW}}=\cos\phi_{\mathrm{SW}}\sin\theta_{\mathrm{SW}} \text{ and } v_{\mathrm{SW}}=\sin\phi_{\mathrm{SW}}\sin\theta_{\mathrm{SW}}. \tag{8b}$$

Here, (θ_{SW}, ϕ_{SW}) is the blindness angle.

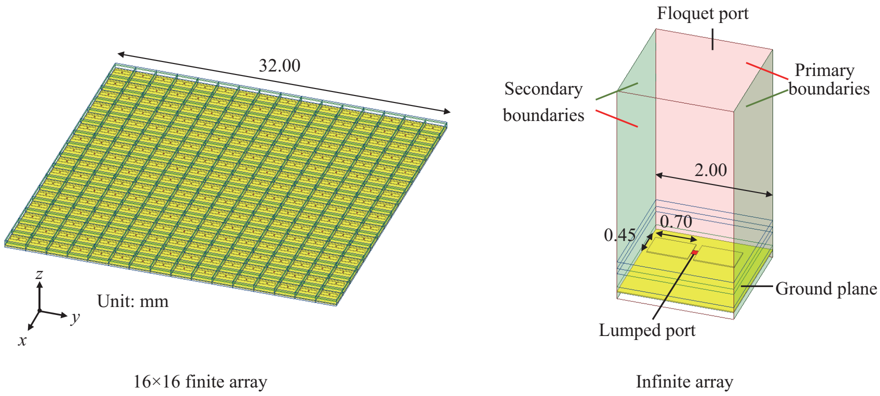

Figure 2 (Color online) Dipole elements in 16 × 16 finite array model and infinite array model.

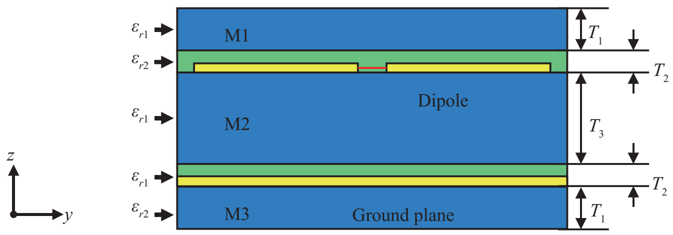

Figure 3 (Color online) PCB stack-ups of infinite dipole array.

2.2 Analysis based on infinite array

As shown in Figure 2, the infinite dipole array is built and analyzed in the full-wave electromagnetic simulation software. The two couples of the airbox faces are set as primary and secondary boundaries, forming the rectangular lattice in Floquet mode analysis. To guarantee the reasonable comparability for the fabricated array prototype by the PCB process, all the models in this subsection use the same configuration of the dielectric layers as shown in Figure 3. Here, the M1 and M2 layers are the superstrate and the substrate for the dipole element, respectively. The dipole radiators are placed on the top of the M2 layer. The M3 layer is added to integrate the feeding network for the antenna experiment. The M1, M2, and M3 layers use the Taconic TLY-5Z laminates ($\varepsilon_{r1} = 2.20$, tan$\delta_1 = 0.0015$), which are bonded by one Rogers RO4450F prepreg layer ($\varepsilon_{r2} = 3.52$, tan $\delta_1 = 0.004$). The detailed parameters are $T_1 = 0.13$ mm, $T_2 = 0.10$ mm, and $T_3 = 0.25$ mm. The dipole is fed by the lumped source with 180 Ω characteristic impedance. Notably, the analysis model takes into account factors such as the mutual coupling and the parasitic reactance between the antenna elements.

The simulated active VSWRs when scanning to (θ_0, ϕ_0) are given in Figure 4. The unacceptable peaks of the active VSWR, i.e., the scanning blindness, occur when scanning to 50° at around 76 GHz and 60° at around 73 GHz in E-plane. To study this phenomenon, the total thickness h and the effective relative permittivity $\varepsilon_{r,\text{eff}}$ of the infinite dipole array can be calculated by

$$h = T_1 + 2T_2 + T_3 = 0.58 \text{ mm}, \tag{9a}$$

$$\varepsilon_{r,\text{eff}} = \frac{\varepsilon_{r1}(T_1 + T_3) + 2\varepsilon_{r2}T_2}{h} \approx 2.66. \tag{9b}$$

Then, considering the highest operating frequency in this design, the β_{SW} can be obtained by solving (4), (6), and (7) with the graphical method as shown in Figure 5. It shows that only the TM mode SW when scanning in E-plane ($\phi_{\text{SW}} = 90°$) can be excited with $\beta_{\text{SW}} \approx 1.20k_0$. By (8), the θ_{SW} is about 50.44° at 76 GHz. The full-wave simulations are taken to verify the theory. As shown in Figure 5(b), the simulated $|S_{11}|$ curves at 76 GHz show the maximum reflection coefficient appears when scanning to $\theta_0 = 50°$ in E-plane, indicating the 0.88% calculation error. With a similar calculation process, the blindness angle at 73 GHz is about 60.09° in calculation and 60° in simulation, indicating the 0.15% calculation error. The simulated radiation patterns at 73 and 76 GHz when scanning in E-plane are shown in Figure 6, showing the scanning blindness as predicted.

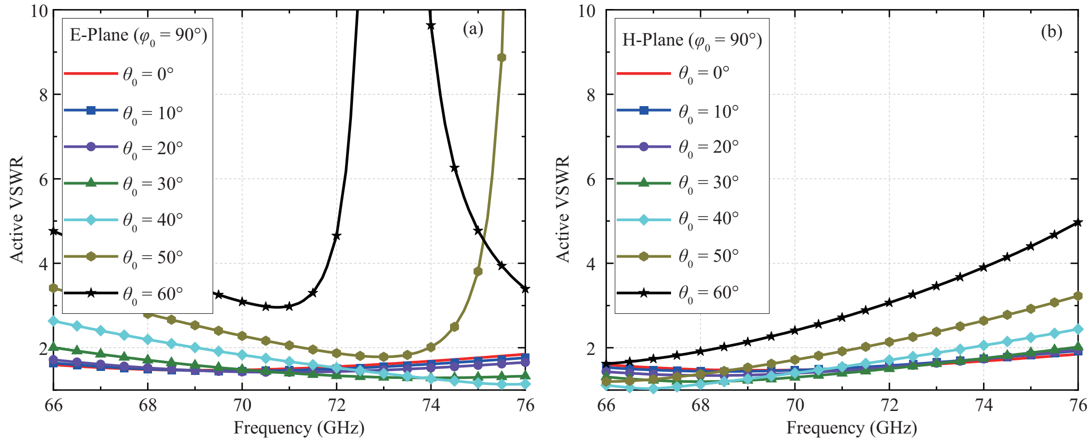

Figure 4 (Color online) Simulated active VSWR for infinite dipole array when scanning. (a) E-plane; (b) H-plane.

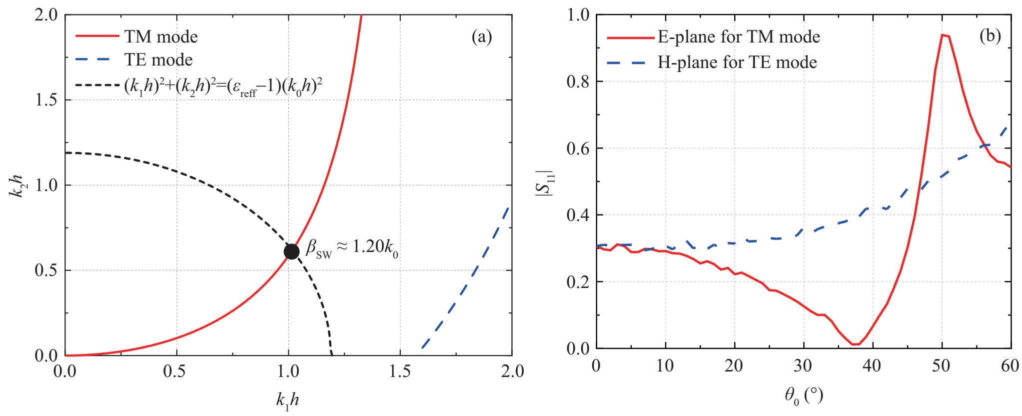

Figure 5 (Color online) Graphical method for obtaining β_{SW} and simulated $|S_{11}|$ versus scanning angle. (a) Graphical method; (b) $|S_{11}|$.

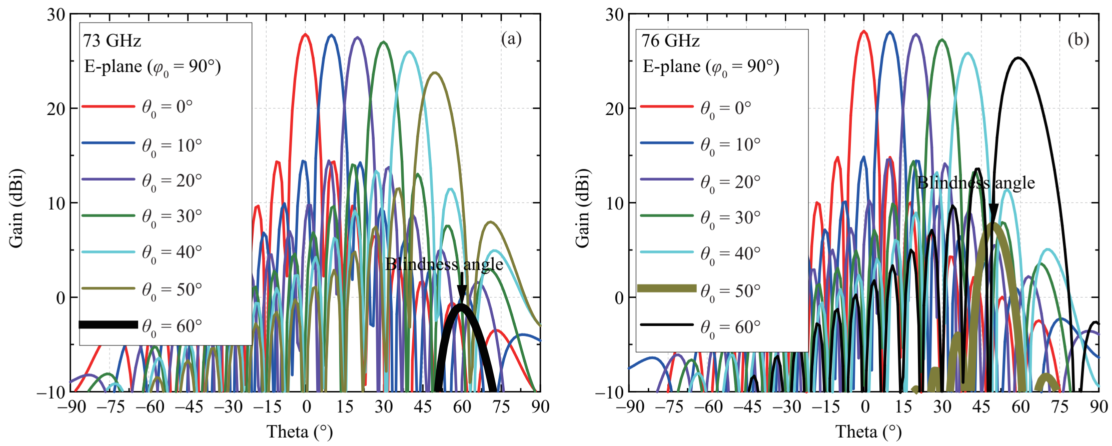

Figure 6 (Color online) Simulated radiation patterns when scanning in E-plane. (a) 73 GHz; (b) 76 GHz.

3 Design of blindness-free beam scanning antenna with AoA architecture for 6G communication systems

3.1 Array topology based on improved maximum-entropy model

The coupling from the radiating Floquet mode to the non-radiation SW mode at the specific scanning angles and frequencies leads to scanning blindness. At the blindness, the propagation constant for the

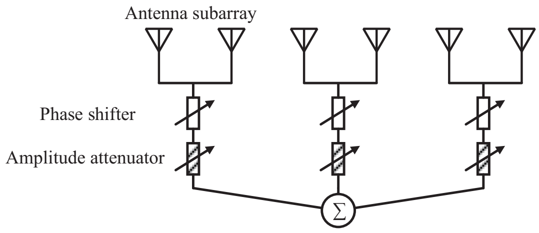

Figure 7 Phased array antenna with AoA architecture consisting of domino subarrays.

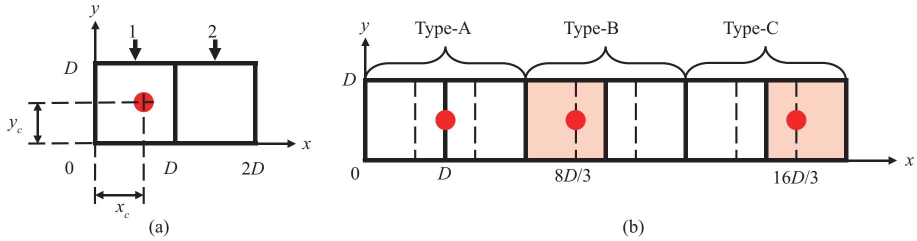

Figure 8 (Color online) Definition and configuration of the equivalent phase center of domino subarray. (a) Definition; (b) configuration.

SW mode is equal to the propagation constant for the Floquet mode by (8). It means the same phase distribution between the inputs in the phased array and the SW along the propagation direction. For the antenna with the AoA architecture consisting of the domino subarrays as shown in Figure 7, the two antenna elements are cophase with the different positions, so that it breaks the one-to-one relations between the phase distribution of the SW mode and the Floquet mode. The periodic subarray reduces the coupling to the SW field and eliminates the blindness. However, it suffers from the high side lobe level or the grating lobe in the desired scanning volume. For an antenna array consisting of the domino-subarray with the $0.5\lambda_{\text{high}}$ element spacing, the grating lobes will appear when scanning over $\pm 30°$ at the highest operating frequency according to the array theory [62]. Here, λ_{high} is the free-space wavelength at the highest operating frequency. It cannot meet the scanning ability requirement for the 6G communication system, which is defined as follows: $\pm 60°$ in a horizontal plane and $\pm 30°$ in a vertical plane.

To suppress the grating lobe, the different inner-phase distributions in the subarrays are introduced for the antenna with the AoA architecture. As shown in Figure 8(a), the equivalent phase center of the domino subarray is defined as (x_c, y_c), which is depended on the phase difference ϕ_c between the inner unit cells of the subarray. ϕ_c is equal to the feeding phase for the element-1 minus the feeding phase for the element-2. Then, it defines that $y_c = D/2$ and $x_c = (1 + \phi_c/\pi)D$. Therefore, when $\phi_{c,A} = 0$, $\phi_{c,B} = -\pi/3$, and $\phi_{c,C} = \pi/3$, the equivalent phase centers of the 1×3 domino subarrays are shown in Figure 8(b). By adding the influence of the inner-phase distributions for the equivalent phase centers into the maximum-entropy model, the entropy of the array in this design can be expressed as

$$H = -\left[\sum_{p=1}^{M} \frac{r_p}{2T}\log_2\left(\frac{r_p}{2T}\right) + \sum_{q=1}^{3N/2} \frac{c_q}{2T}\log_2\left(\frac{c_q}{2T}\right)\right] = -(H_r + H_c), \tag{10a}$$

$$T = MN/2. \tag{10b}$$

Here, M and N are the mark numbers for the row and column of the array along the y- and x-direction, respectively. Due to that (x_c, y_c) may be not the integer coordinate, the grids are subdivided for p-row ($p = 1, 2, \ldots, M$) and q-column ($q = 1, 2, \ldots, 3N/2$). r_p and r_q are the number of the phase center on the p-row and q-column, respectively. H_r and H_c are the contributions for entropy in rows and columns, respectively. By setting the number of phase centers on each row to be identical and the same as for each column, the upper limit of the entropy of the array can be expressed as

$$H_{\max} = -\frac{1}{2}\left[\log_2\left(\frac{1}{2M}\right) + \log_2\left(\frac{1}{3N}\right)\right]. \tag{11}$$

When setting the proportion of the subarrays with or without the inner-phase distributions to p_1 and

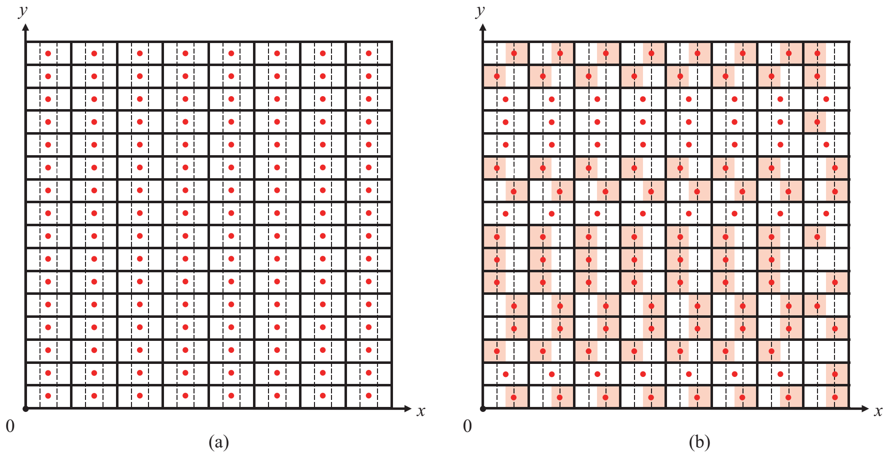

Figure 9 (Color online) 16 × 16 array topology. (a) Before optimization; (b) after optimization.

p_2, the array topology can be obtained by solving the optimization problem as

$$\min : H_{\max} - H \tag{12a}$$
$$\text{s.t.} \quad p_1 + p_2 = 1. \tag{12b}$$

The invasive weed optimization (IWO) algorithm [64] is employed to enumerate all possible array topologies and obtain the optimal array topology by (12). The obtained array topology is not only one and not necessarily effective for the wide-scanning requirement so it needs to be screened further. With the fixed array topology, the array pattern can be expressed as

$$E(\theta,\phi) = \sum_{t=1}^{T} I_t e_t \mathrm{e}^{\mathrm{j}k_0(x_t \sin\theta\cos\phi + y_t \sin\theta\sin\phi)}. \tag{13}$$

In (13), I_t, e_t, and (x_t, y_t) are the complex excitation, the embedded pattern, and the coordinate for the subarray t. The I_t can be obtained by solving the convex optimization problem with the desired side lobe level. When there is no solution to the convex optimization problem, the values of p_1 and p_2 in the IWO algorithm should be adjusted.

3.2 Analysis based on finite array

The array with 16 × 16 antenna elements will be built and discussed. As the wide-scanning requirement for the 6G base station, the phased array antenna needs to obtain the beam coverage over ±60° in a horizontal plane and ±30° in a vertical plane. It can increase p_2 due to the larger periodicity allowed for the smaller scanning range along the x-direction. The lesser phase-shifting subarrays in the whole array are hoped to reduce the additional insertion loss induced by the phase-shifting networks. Therefore, the array is demanded for scanning to ±60° along the y-direction and ±30° along the x-direction as shown in Figure 9(a). After the optimization mentioned above, the array topology with $p_1 = 0.75$ and $p_2 = 0.25$ is shown in Figure 9(b). Here, the co-polarization in the E-plane of the dipole elements is arrayed along the y-direction.

To further validate this design, the configuration of the dipole element with the feedline is shown in Figure 10(a) with the detailed structure parameters. The PCB stack-ups for the antenna element with the feedline are the same as the infinite array model as shown in Figure 3. In addition, the MS is placed on the top of the M1 layer for improving the impedance matching. The evolution procedures are given in Figure 10(b). To study the performance of the impedance and the mutual coupling for the antenna following the evolution procedures, the simulated S-parameters are shown in Figure 11, including the reflection coefficients of the central element and transmission coefficients between the central element and the surrounding elements. Compared to the initial model, the final model shows a better impedance matching with the reflection coefficient lower than −11.09 dB. The worst transmission coefficient, i.e., the worst isolation, is also improved from −11.31 to −11.97 dB. Here, the worst isolation is always the isolation between the central element and its two adjacent elements in the E-plane. The simulated central

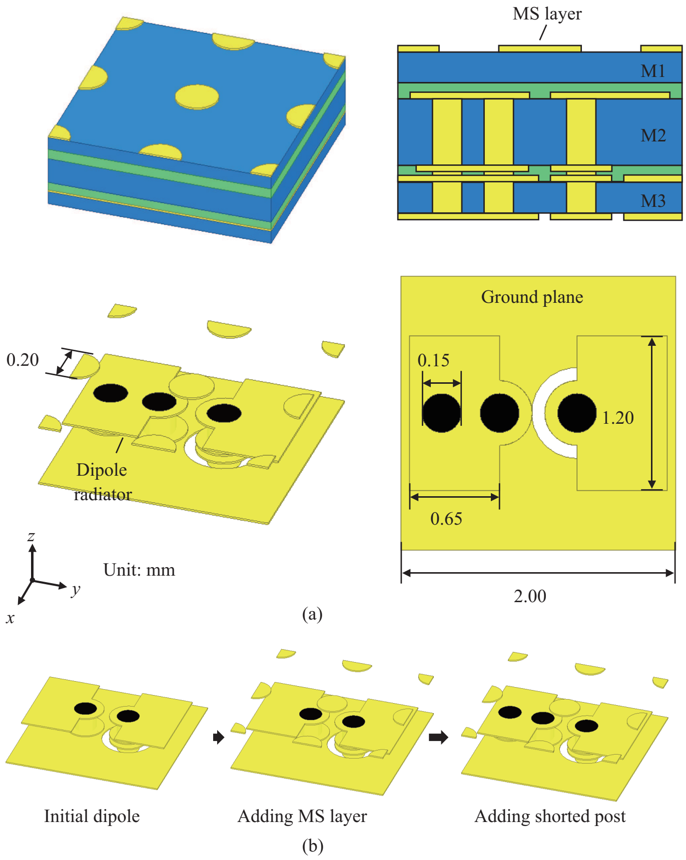

Figure 10 (Color online) Configuration of the dipole element with the feedline and the evolution procedures. (a) Configuration; (b) evolution procedures.

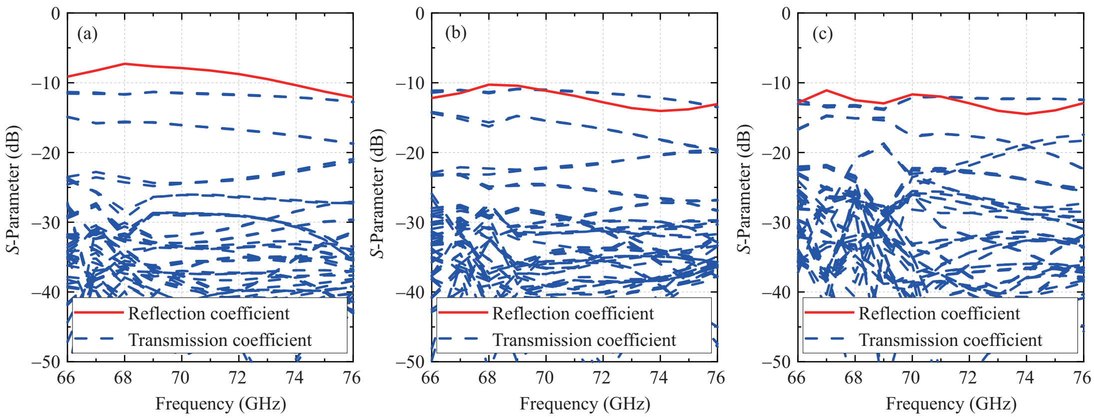

Figure 11 (Color online) Simulated S-parameters for the antenna following the evolution procedures. (a) Initial dipole; (b) adding MS layer; (c) adding a shorted post.

embedded element patterns in the E-plane at the center operating frequency following the evolution procedures are shown in Figure 12. Compared to the initial model, the radiation pattern of the final model shows a wider beamwidth, which indicates better beam coverage [36]. Therefore, these modifications, including the addition of the MS and the shorted post for the initial dipole element, improve the impedance matching and eliminate the distortion of the element pattern caused by the mutual coupling.

After the full wave analysis for the final 16 × 16 array antenna, the simulated radiation patterns at 73 and 76 GHz are shown in Figure 13. The simulated gains at broadside are 28.18 and 28.42 dBi at 73 and 76 GHz, respectively. It shows that the slight gain loss when scanning to broadside exists in the optimized topology, compared to the ideal gain $G_{\text{ideal}} = 10\log_{10}(4\pi S/\lambda_0^2)\cos\theta_0$. Here, $S = 32\text{mm} \times 32$ mm is the

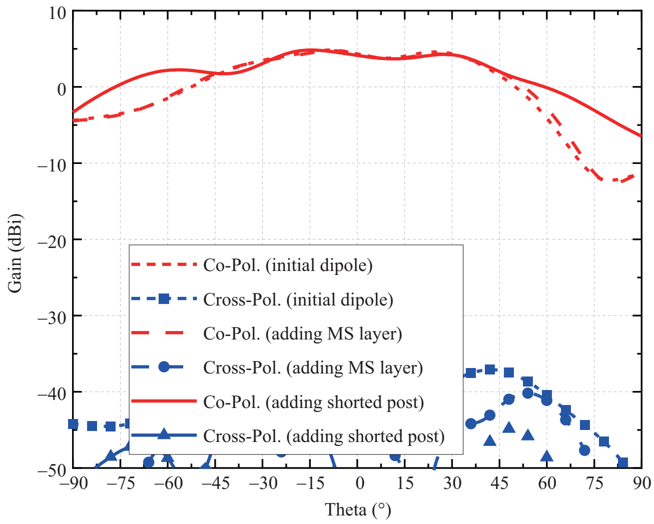

Figure 12 (Color online) Simulated central embedded element patterns following the evolution procedures.

area of the array. G_{ideal} is 28.81 and 29.16 dBi at 73 and 76 GHz when scanning to the broadside, respectively. It shows that the simulated radiation efficiency is about 86.49% and 84.33% at 73 and 76 GHz when scanning to the broadside, respectively. That is because the tilted subarray patterns are caused by the inner-phase distributions. However, the sacrifice is worth it. These tilted subarray patterns are beneficial for scanning out of the broadside and suppressing the grating lobe along the x-direction. The simulated radiation patterns for the antenna with the array topology shown in Figure 9(a) are brought in for reference. At the highest operating frequency, the simulated gains are 25.17 and 24.01 dBi when scanning to 50° and 30° in E-plane and H-plane, respectively. By the theoretical calculations, the simulated radiation efficiency is better than 62.08% when scanning in the E-plane and is better than 35.23% when scanning in the H-plane, respectively. Obviously, there is a significant efficiency reduction when scanning, especially for scanning in H-plane. That is because even though the original grating lobe is suppressed, the more radiated power is still allocated to the side lobe region of the antenna array pattern, compared to the unit-level array antenna with the $0.5\lambda_{\text{high}}$ element spacing. As a benefit, in E-plane, the blindness is eliminated when scanning to 60° at 73 GHz and 50° at 76 GHz. In H-plane, the grating lobe is suppressed and the side lobe levels are lower than -11.82 dB when scanning to 30°.

4 Experimental results and discussion

The 16 × 16 array phototypes are built and fabricated by the multi-layer PCB process to verify the theory and simulation, as shown in Figures 14(a) and (b). Notably, the feeding network of the measured array is designed based on the substrate-integrated waveguide (SIW) transmission lines. The dipole element is fed by the grounded coplanar waveguide (GCPW). As shown in Figures 14(c) and (d), the transition from SIW to GCPW is designed to interconnect the dipole element and the feeding network. Figure 14(e) shows the interconnection of the dipole elements and the feeding network. The central 2 × 16 dipole elements are excited when the surrounding dipole elements are shorted to the ground plane. The feeding posts of the dipole elements pass through the ground plane and connect with the GCPW on the bottom layer. Finally, the SIW-to-GCPW transitions are used to connect the 1-to-32 power divider to the 2 × 16 dipole elements. Considering that it is very complicated to simultaneously control the amplitude and phase of the feed network, the complex excitation for each channel of the measured array is optimized by the phase-only synthesis technology [65]. Therefore, the deterioration of the side lobe level for scanning in the H-plane is inevitable. Then, as shown in Figure 14(d), the desired phase-only excitations are implemented by the equal-length and unequal-width phase shifters [66]. The unequal width is based on adjusting the positions of the shorted posts for the SIW transmission lines. The central 2 × 16 arrays, i.e., the central 1 × 16 subarray, are actually measured for evaluating the performance when scanning to (θ_0, ϕ_0). The antenna elements are unit-levelly fed by the SIW-based feeding networks. The SIW-to-waveguide transition fabricated by the aluminum plates is added to form the feed waveguide.

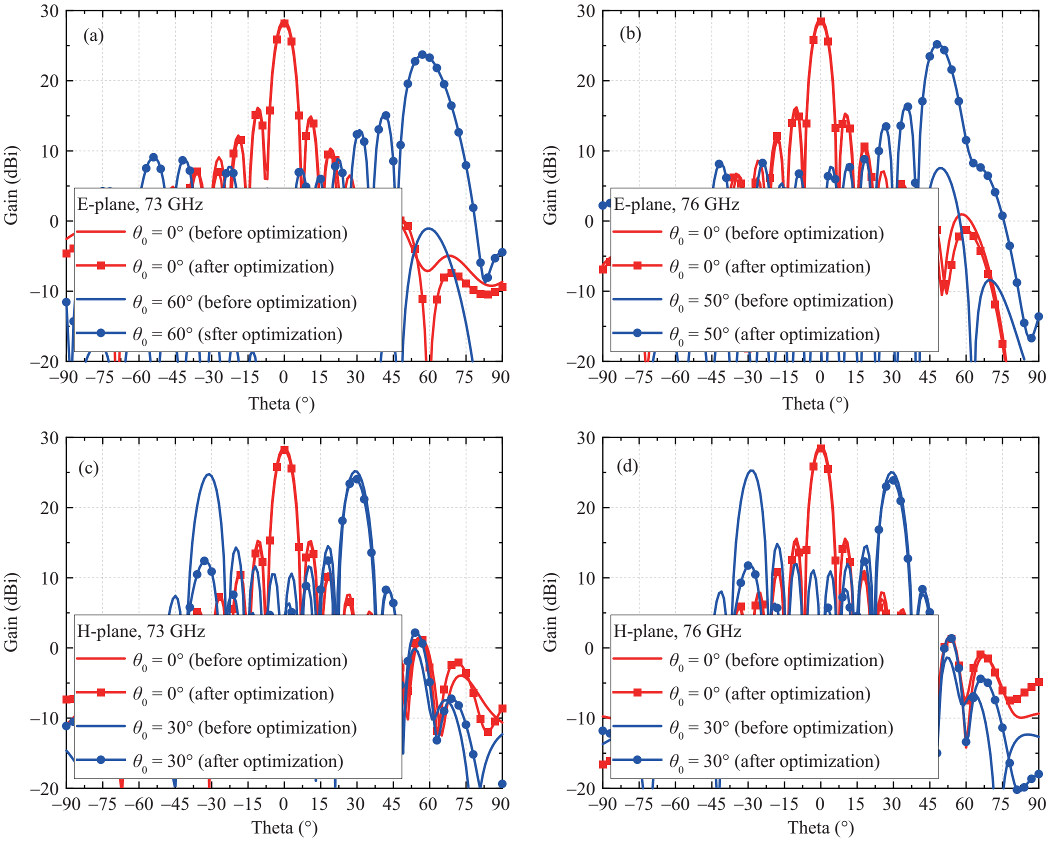

Figure 13 (Color online) Simulated patterns of 16 × 16 array antenna. (a) 73 GHz in E-plane; (b) 76 GHz in E-plane; (c) 73 GHz in H-plane; (d) 76 GHz in H-plane.

The measured and simulated VSWRs for the array prototype when scanning to broadside are shown in Figure 15. It is fed by the same feeding network when scanning to broadside for all the frequencies. Notably, the measured 1 × 16 subarray with the broadside configuration is composed of the dipole elements which are arrayed along the co-polarization direction. The VSWRs are lower than 1.76 at the broadside. To simplify the experiment, the capacity of the elimination for the scanning blindness and the suppression for the grating lobe is verified at the highest operating frequency, i.e., 76 GHz. For the highest operating frequency, the scanning blind caused by the SW can be seen when scanning to 50° in E-plane, according to the simulated result in Figure 5. Due to the sparsely-excited configuration along the H-plane in this design, the theoretically highest side lobe or nearest grating lobe will appear when scanning to 30° at 76 GHz. The measured and simulated VSWRs of the array prototypes with the different feeding networks for scanning to 50° in E-plane and 30° in H-plane are also added in Figure 15. It remains lower than 2.87 and 2.16 when scanning to 50° in E-plane and 30° in H-plane, respectively. It shows a good agreement between the simulated and measured results.

However, it is undeniable that the good impedance characteristic of the array with the feeding network is not enough to prove the good performance. On the one hand, the additional insertion loss is induced by the feeding network. On the other hand, the feeding network also acts as an impedance transformer. To further verify the performance of the proposed array antenna, the radiation patterns are measured and compared with the simulations. Meanwhile, to calibrate and compensate for the introduced insertion loss by the feeding networks, the transmission lines and the transitions are also fabricated and measured. As shown in Figure 16, the radiation patterns are given when scanning to broadside at 66, 71, and 76 GHz. As shown in Figure 17, the scanning patterns are sampled at 76 GHz when scanning to 50° in the E-plane and 30° in the H-plane, respectively. There is no distinct gain drop in the main lobe when scanning to 50° at 76 GHz in the E-plane, which indicates that the scanning blindness is successfully eliminated. At the same time, there is no existence of the grating lobe when scanning to 30° at 76 GHz in the H-plane, which indicates the efficiency of the improved maximum-entropy model. The measured radiation patterns have some deteriorations and differences in the side lobe regions. The amplitude and phase differences

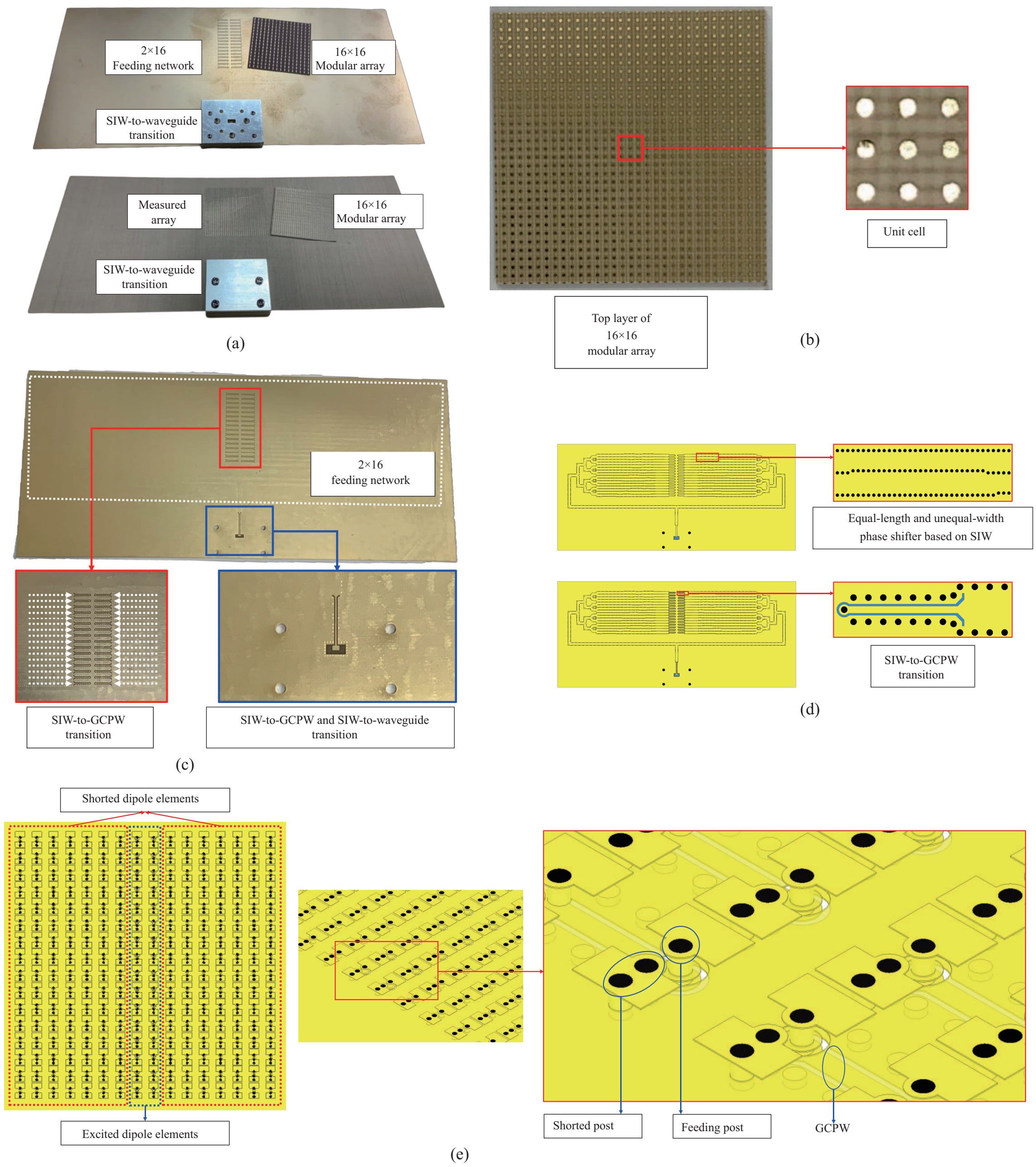

Figure 14 (Color online) Array prototype. (a) Measured array; (b) modular array; (c) feeding network; (d) detailed structures of feeding network; (e) interconnection of dipole elements and feeding network.

in each channel of the feeding network, which are mainly caused by the fabricated tolerance of the multi-layer PCB process, can lead to these. The broadside gain versus frequency is given in Figure 18. The calculated ideal gain is brought in for reference. The theoretical co-polarization gain is given by $G_{\text{ideal}} = 10\log_{10}(4\pi S/\lambda_0^2)\cos\theta_0)$. The measured cross-pol. level is lower than -29.71 dB. There are some discrepancies between the measured and simulated co-/cross-polarization gain curves. The assembly and position errors in the antenna experiment can lead to these discrepancies.

Table 1 gives the comparison between the proposed antenna and the other state-of-the-art studies. The sparsely-excited phased array antenna with the AoA architecture and the improved maximum-entropy model are employed in this design to eliminate the scanning blindness and suppress the grating lobe. Therefore, the proposed antenna achieves wide beam coverage with the blindness free and grating-lobe free performance. In addition, the 51.30% channel reduction is also achieved compared to the uniform array.

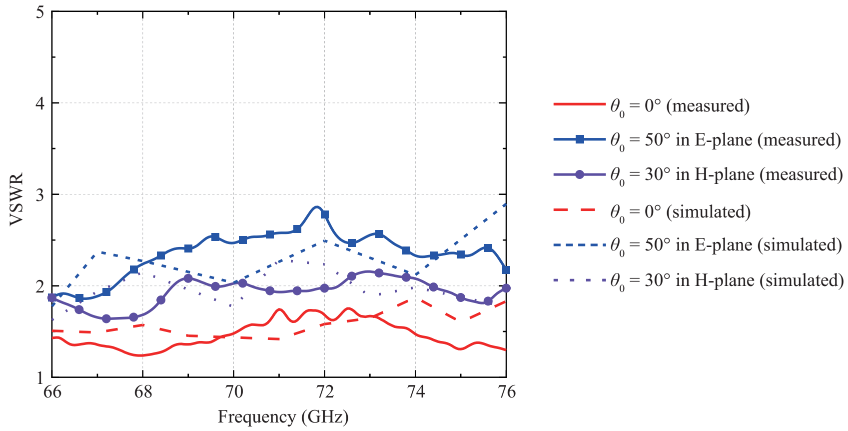

Figure 15 (Color online) Measured and simulated VSWRs results.

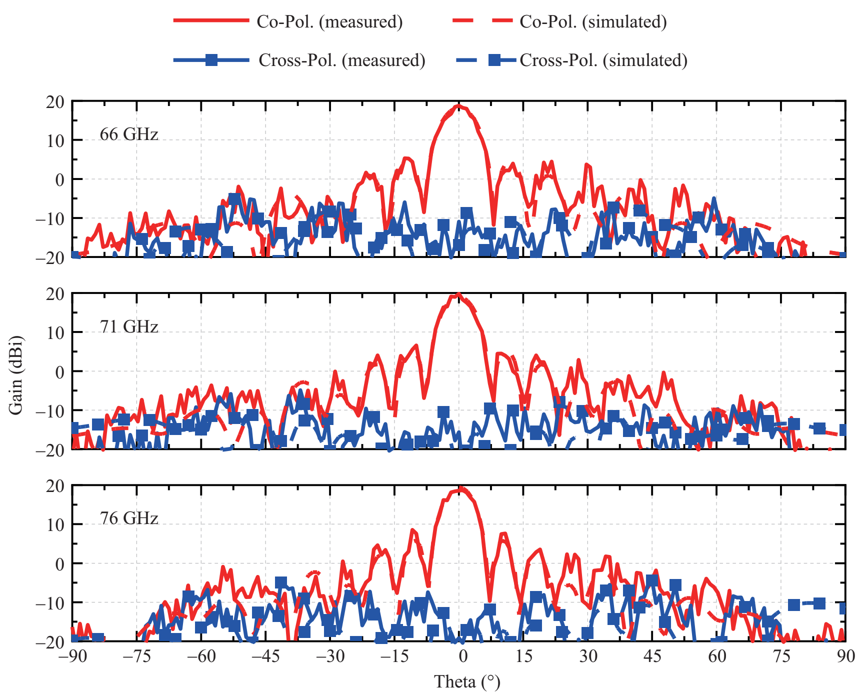

Figure 16 (Color online) Measured and simulated radiation patterns when scanning to broadside.

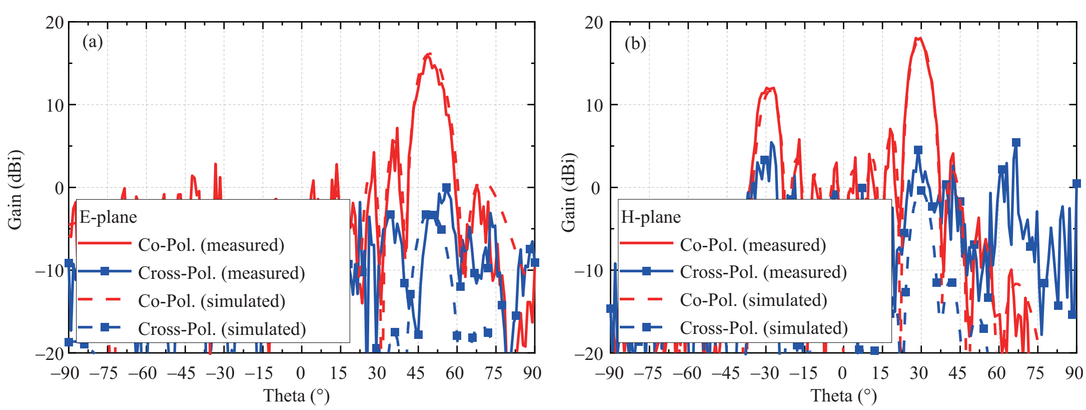

Figure 17 (Color online) Measured and simulated radiation patterns when scanning to (a) 50° in E-plane and (b) 30° in H-plane.

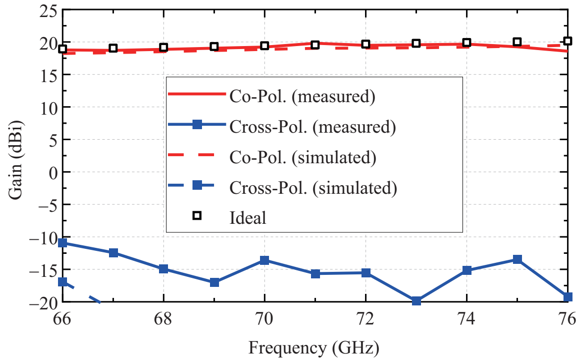

Figure 18 (Color online) Measured and simulated broadside gains.

Table 1 Performance comparison between different phased arrays

Ref.	Impedance bandwidth (GHz)	Scanning range (E/H)	Channel number (%)*	Method to suppress blindness	Fabrication process	Type of element	Design complexity
[34]	4.87–5.84	±30°/±30°	−24.37	Uniplanar compact EBG	PCB	Patch	Normal
[33]	8–12	±60°/±60°	−17.67	Mushroom-like EBG	PCB and machining process	Backed-Cavity Patch	Normal
[41]	8–12	±60°/±60°	−15.22	Subarray technology	PCB	Dipole	Difficult
[36]	7–21	±45°/±45°	+17.12	Air-filled perforations	PCB	Dipole	Normal
[13]	22–27	±45°/±45°	+2.03	Not applicable	PCB	Backed-Cavity patch	Simple
[11]	57–66	±45°/±45°	+6.72	Not applicable	LTCC	Patch	Simple
[25]	56–67	±30°/±30°	−19.80	Not applicable	LTCC	Patch	Simple
This work	66–76	±60°/±30°	−51.30	Subarray technology	PCB	Dipole	Difficult

* It is defined as the ratio between the used number of the channels and the theoretical number of the channels. The theoretical number of the channels is defined when the antenna elements are located to the rectangular grid with the $0.5\lambda_{\rm high}$ spacing both in E-plane and H-plane. Therefore, the negative ratio refers to the reduced number of the channels, when the positive ratio refers to the increased number of the channels.

5 Conclusion

A new method has been developed for eliminating the scanning blindness caused by the SW. A sparsely-excited phased array antenna is proposed with AoA architecture with two types of domino subarrays. The topology of this aperiodic array is optimized by the improved maximum entropy model. Therefore, the coupling from the radiating Floquet modes to the non-radiating SW modes is broken by the uniform inner-phase distribution of the array. At the same time, although the element spacing is more than $1\lambda_{\rm high}$ in H-plane, the grating lobe is also suppressed inside the scanning volume due to the aperiodic array topology. The simulated and measured results show that the array prototype can achieve the operating bandwidth from 66 to 76 GHz with a 51.30% channel reduction. The array prototype also achieves the beam coverage of ±60° in the E-plane and ±30° in the H-plane without incurring either scanning blindness or grating lobe. It provides a promising method for developing the 6G high-integrated phased array antenna at the millimeter-wave bands.

Acknowledgements This work was supported in part by National Key Research and Development Plan of China (Grant No. 2020YFB1807404).

References

1 You X H, Wang C X, Huang J, et al. Towards 6G wireless communication networks: vision, enabling technologies, and new paradigm shifts. Sci China Inf Sci, 2021, 64: 110301
2 Zhao J, Nie Y, Zhang H, et al. Decision intelligence empowered resource management for 6G vehicle-to-everything communications. Chinese J Electron, 2023, in press
3 Wang Z Q, Du Y, Wei K J, et al. Vision, application scenarios, and key technology trends for 6G mobile communications. Sci China Inf Sci, 2022, 65: 151301
4 Guo Q Y, Wong H. Design of an air-filled slot antenna and array for millimeter-wave applications. IEEE Trans Antennas Propagat, 2022, 70: 7217–7222
5 Liu P, Pedersen G F, Zhang S. Wideband low-sidelobe slot array antenna with compact tapering feeding network for E-band wireless communications. IEEE Trans Antennas Propagat, 2022, 70: 2676–2685

6 Wang C, Hou D B, Zheng S D, et al. E-band transceiver monolithic microwave integrated circuit in a waveguide package for millimeter-wave radio channel emulation applications. Sci China Inf Sci, 2022, 65: 129404
7 Chi L, Weng Z, Qi Y, et al. A 60 GHz PCB wideband antenna-in-package for 5G/6G applications. Antennas Wirel Propag Lett, 2020, 19: 1968–1972
8 Kindt R W, Binder B T. Wideband, low-profile, dual-polarized machined-metal array on a triangular lattice. IEEE Trans Antennas Propagat, 2022, 70: 1097–1106
9 Tianang E G, Elmansouri M A, Filipovic D S. Ultrawideband flush-mountable dual-polarized Vivaldi antenna. IEEE Trans Antennas Propagat, 2020, 68: 5670–5674
10 Elmansouri M A, Friedrichs G R, Boskovic L B, et al. An X-band through Ka-band thinned all-metal Vivaldi phased array. IEEE Trans Antennas Propagat, 2021, 69: 7613–7623
11 Hong W, Goudelev A, Baek K, et al. 24-element antenna-in-package for stationary 60-GHz communication scenarios. Antennas Wirel Propag Lett, 2011, 10: 738–741
12 Liu H Q, Zhao D X, Yi Y R, et al. A 24.25-27.5 GHz 128-element dual-polarized 5G integrated phased array with 5.6%-EVM 400-MHz 64-QAM and 50-dBm EIRP. Sci China Inf Sci, 2022, 65: 214301
13 Guo J, Hu Y, Hong W. A 45° polarized wideband and wide-coverage patch antenna array for millimeter-wave communication. IEEE Trans Antennas Propagat, 2022, 70: 1919–1930
14 Sun J X, Cheng Y J, Fan Y. Planar ultra-wideband and wide-scanning dual-polarized phased array with integrated coupled-marchand balun for high polarization isolation and low cross-polarization. IEEE Trans Antennas Propagat, 2021, 69: 7134–7144
15 Ding Y R, Cheng Y J. A tri-band shared-aperture antenna for (2.4, 5.2) GHz Wi-Fi application with MIMO function and 60 GHz Wi-Gig application with beam-scanning function. IEEE Trans Antennas Propagat, 2020, 68: 1973–1981
16 Wang H B, Cheng Y J. Single-layer dual-band linear-to-circular polarization converter with wide axial ratio bandwidth and different polarization modes. IEEE Trans Antennas Propagat, 2019, 67: 4296–4301
17 Alibakhshikenari M, Ali E M, Soruri M, et al. A comprehensive survey on antennas on-chip based on metamaterial, metasurface, and substrate integrated waveguide principles for millimeter-waves and terahertz integrated circuits and systems. IEEE Access, 2022, 10: 3668–3692
18 Zhang Y P, Liu D X. Antenna-on-chip and antenna-in-package solutions to highly integrated millimeter-wave devices for wireless communications. IEEE Trans Antennas Propagat, 2009, 57: 2830–2841
19 Althuwayb A A, Alibakhshikenari M, Virdee B S, et al. Antenna on chip (AoC) design using metasurface and SIW technologies for THz wireless applications. Electronics, 2021, 10: 1120
20 Alibakhshikenari M, Virdee B S, Althuwayb A A, et al. Compact and low-profile on-chip antenna using underside electromagnetic coupling mechanism for terahertz front-end transceivers. Electronics, 2021, 10: 1264
21 Shin W, Ku B H, Inac O, et al. A 108-114 GHz 4×4 wafer-scale phased array transmitter with high-efficiency on-chip antennas. IEEE J Solid-State Circ, 2013, 48: 2041–2055
22 Caster F, Gilreath L, Pan S, et al. Design and analysis of a W-band 9-element imaging array receiver using spatial-overlapping super-pixels in silicon. IEEE J Solid-State Circ, 2014, 49: 1317–1332
23 Alibakhshikenari M, Virdee B S, Khalily M, et al. High-gain on-chip antenna design on silicon layer with aperture excitation for terahertz applications. Antennas Wirel Propag Lett, 2020, 19: 1576–1580
24 Shahramian S, Holyoak M J, Baeyens Y. A 16-element W-band phased-array transceiver chipset with flip-chip PCB integrated antennas for multi-gigabit wireless data links. IEEE Trans Microwave Theor Techn, 2018, 66: 3389–3402
25 Rashidian A, Jafarlou S, Tomkins A, et al. Compact 60 GHz phased-array antennas with enhanced radiation properties in flip-chip BGA packages. IEEE Trans Antennas Propagat, 2019, 67: 1605–1619
26 Zhou C, Yang W, Xue Q, et al. Millimeter-wave wideband dual-polarized LTCC antenna array based on metasurfaces for beam-scanning applications. IEEE Trans Antennas Propagat, 2022, 70: 9912–9917
27 Gu X, Liu D, Baks C, et al. Development, implementation, and characterization of a 64-element dual-polarized phased-array antenna module for 28-GHz high-speed data communications. IEEE Trans Microwave Theor Techn, 2019, 67: 2975–2984
28 Hong W, Baek K, Goudelev A. Grid assembly-free 60-GHz antenna module embedded in FR-4 transceiver carrier board. IEEE Trans Antennas Propagat, 2013, 61: 1573–1580
29 Li R, Jin C, Ong S C, et al. Embedded wafer level packaging for 77-GHz automotive radar front-end with through silicon via and its 3-D integration. IEEE Trans Compon Packag Manufact Technol, 2013, 3: 1481–1488
30 Pozar D, Schaubert D. Scan blindness in infinite phased arrays of printed dipoles. IEEE Trans Antennas Propagat, 1984, 32: 602–610
31 Donzelli G, Capolino F, Boscolo S, et al. Elimination of scan blindness in phased array antennas using a grounded-dielectric EBG material. Antennas Wirel Propag Lett, 2007, 6: 106–109
32 Fu Y Q, Yuan N C. Elimination of scan blindness in phased array of microstrip patches using electromagnetic bandgap materials. Antennas Wirel Propag Lett, 2004, 3: 63–65
33 Zou W M, Qu S W, Yang S. Wideband wide-scanning phased array in triangular lattice with electromagnetic bandgap structures. Antennas Wirel Propag Lett, 2019, 18: 422–426
34 Iluz Z, Shavit R, Bauer R. Microstrip antenna phased array with electromagnetic bandgap substrate. IEEE Trans Antennas Propagat, 2004, 52: 1446–1453
35 Holland S S, Vouvakis M N. The planar ultrawideband modular antenna (PUMA) array. IEEE Trans Antennas Propagat, 2012, 60: 130–140
36 Holland S S, Schaubert D H, Vouvakis M N. A 7-21 GHz dual-polarized planar ultrawideband modular antenna (PUMA) array. IEEE Trans Antennas Propagat, 2012, 60: 4589–4600
37 Sun J X, Cheng Y J. Dual-polarized Ka-band phased array using hybrid magnetic-/electric-dipole with low profile for low cross-polarization leakage inside $\pm 60^\circ$ scan volume. IEEE Trans Antennas Propagat, 2023, 71: 4204–4215
38 Pozar D M. Scanning characteristics of infinite arrays of printed antenna subarrays. IEEE Trans Antennas Propagat, 1992, 40: 666–674
39 Rocca P, Oliveri G, Mailloux R J, et al. Unconventional phased array architectures and design methodologies — a review. Proc IEEE, 2016, 104: 544–560
40 Rupakula B, Aljuhani A H, Rebeiz G M. Limited scan-angle phased arrays using randomly grouped subarrays and reduced number of phase shifters. IEEE Trans Antennas Propagat, 2020, 68: 70–80
41 Ma Y, Yang S, Chen Y, et al. Sparsely excited tightly coupled dipole arrays based on irregular array techniques. IEEE Trans Antennas Propagat, 2020, 68: 6098–6108

42 Ma Y, Yang S, Chen Y, et al. High-directivity optimization technique for irregular arrays combined with maximum entropy model. IEEE Trans Antennas Propagat, 2021, 69: 3913–3923
43 Ma Y, Yang S. A phase compensation technique for the tradeoff design of irregular phased array. In: Proceedings of IEEE International Symposium on Antennas and Propagation and USNC-URSI Radio Science Meeting (APS/URSI), Singapore, 2021. 783–784
44 Mou L W, Cheng Y J. Design of aperiodic subarrayed phased arrays with structural repetitiveness. IEEE Trans Antennas Propagat, 2022, 70: 11697–11706
45 Alibakhshikenari M, Babaeian F, Virdee B S, et al. A comprehensive survey on "various decoupling mechanisms with focus on metamaterial and metasurface principles applicable to SAR and MIMO antenna systems". IEEE Access, 2020, 8: 192965
46 Alibakhshikenari M, Khalily M, Virdee B S, et al. Mutual coupling suppression between two closely placed microstrip patches using EM-bandgap metamaterial fractal loading. IEEE Access, 2019, 7: 23606–23614
47 Alibakhshikenari M, Khalily M, Virdee B S, et al. Mutual-coupling isolation using embedded metamaterial EM bandgap decoupling slab for densely packed array antennas. IEEE Access, 2019, 7: 51827–51840
48 Bouknia M L, Zebiri C, Sayad D, et al. Analysis of the combinatory effect of uniaxial electrical and magnetic anisotropy on the input impedance and mutual coupling of a printed dipole antenna. IEEE Access, 2021, 9: 84910–84921
49 Wang Z, Wu Q. A novel decoupling feeding network for circularly polarized patch arrays using orthogonal mode decomposition. IEEE Trans Antennas Propagat, 2023, 71: 1448–1457
50 Wu K L, Wei C, Mei X, et al. Array-antenna decoupling surface. IEEE Trans Antennas Propagat, 2017, 65: 6728–6738
51 Zhu Y, Chen Y, Yang S. Cross-band mutual coupling reduction in dual-band base-station antennas with a novel grid frequency selective surface. IEEE Trans Antennas Propagat, 2021, 69: 8991–8996
52 Guo J, Liu F, Zhao L, et al. Partial reflective decoupling superstrate for dual-polarized antennas application considering power combining effects. IEEE Trans Antennas Propagat, 2022, 70: 9855–9860
53 Sun L, Li Y, Zhang Z, et al. Antenna decoupling by common and differential modes cancellation. IEEE Trans Antennas Propagat, 2021, 69: 672–682
54 Sun L, Li Y, Zhang Z. Decoupling between extremely closely spaced patch antennas by mode cancellation method. IEEE Trans Antennas Propagat, 2021, 69: 3074–3083
55 Odabasi H, Salimitorkamani M, Turan G. Mutual coupling reduction between closely placed patch antennas using complementary U-shaped polarization converter. Antennas Wirel Propag Lett, 2023, 22: 2710–2714
56 Song W, Zhu X W, Wang L, et al. Simple structure E-plane decoupled millimeter wave antenna based on current cancellation model. IEEE Trans Antennas Propagat, 2022, 70: 9871–9876
57 Guo C, Li J, Yang D, et al. Compact co-polarized decoupled microstrip patch array antenna based on TM_02/TM_03 modes cancellation. IEEE Trans Antennas Propagat, 2022, 70: 9906–9911
58 Qian J F, Gao S, Sanz-Izquierdo B, et al. Mutual coupling suppression between two closely placed patch antennas using higher-order modes. IEEE Trans Antennas Propagat, 2023, 71: 4686–4694
59 Cheung S K, Halloran T P, Weedon W H, et al. MMIC-based quadrature hybrid quasi-circulators for simultaneous transmit and receive. IEEE Trans Microwave Theor Techn, 2010, 58: 489–497
60 Dash J C, Sarkar D. A colinearly polarized full-duplex antenna with extremely high Tx-Rx isolation. Antennas Wirel Propag Lett, 2022, 21: 2387–2391
61 Doane J P, Sertel K, Volakis J L. Matching bandwidth limits for arrays backed by a conducting ground plane. IEEE Trans Antennas Propagat, 2013, 61: 2511–2518
62 Balanis C A. Antenna Theory: Analysis and Design. 3rd ed. Hoboken: John Wiley & Sons, 2005
63 Pozer D M. Microwave Engineering. 4th ed. Hoboken: John Wiley & Sons, 2011
64 Mehrabian A R, Lucas C. A novel numerical optimization algorithm inspired from weed colonization. Ecol Inf, 2006, 1: 355–366
65 Fuchs B. Application of convex relaxation to array synthesis problems. IEEE Trans Antennas Propagat, 2014, 62: 634–640
66 Cheng Y J, Hong W, Wu K. Broadband self-compensating phase shifter combining delay line and equal-length unequal-width phaser. IEEE Trans Microwave Theor Techn, 2010, 58: 203–210